

Article

Multiport Energy Management System Design for a 150 kW Range-Extended Towing Vessel

Yachao Zhu ^{1,*}, Hao Wang ^{2,*}, Yuanyang Liu ¹, Gang Lei ^{1,*} and Jianguo Zhu ³

¹ School of Electrical and Data Engineering, University of Technology Sydney, Ultimo, NSW 2007, Australia; liuyuanyangrex@gmail.com

² Department of Microelectronics Engineering, Wanjiang College, Anhui Normal University, Wuhu 241002, China

³ School of Electrical and Information Engineering, University of Sydney, Camperdown, NSW 2006, Australia; jianguo.zhu@sydney.edu.au

* Correspondence: yachao.zhu-1@student.uts.edu.au (Y.Z.); warmhow7777@gmail.com (H.W.); gang.lei@uts.edu.au (G.L.)

† These authors contributed equally to this work.

Abstract: This paper proposes a multiport energy management system (EMS) and its rule-based expert control strategy for a 150 kW range-extended towing vessel (RETV). The system integrates a diesel generator system, a permanent magnet synchronous motor, a lithium battery, and supercapacitors. To verify its feasibility and effectiveness, the proposed multiport EMS was modelled and tested through MATLAB/Simulink. Simulation results demonstrate that the designed multiport EMS works efficiently under the five typical operating conditions of the 150 kW RETV. In addition, two case studies were conducted and compared to investigate the impact of the battery's initial state of charge (SoC) on the system's energy efficiency. It was found that an overall 85% energy efficiency can be achieved for the RETV when the initial SoC is either 75% or 15%. The battery consistently operates within the optimal SoC range of 20% to 80%, and the supercapacitors effectively meet the instantaneous high-power demand.

Keywords: energy management system; energy efficiency; towing vessel; battery; expert control strategy



Citation: Zhu, Y.; Wang, H.; Liu, Y.; Lei, G.; Zhu, J. Multiport Energy Management System Design for a 150 kW Range-Extended Towing Vessel. *Appl. Sci.* **2023**, *13*, 12933. <https://doi.org/10.3390/app132312933>

Academic Editor: Paweł Szcześniak

Received: 24 October 2023

Revised: 1 December 2023

Accepted: 2 December 2023

Published: 3 December 2023



Copyright: © 2023 by the authors. Licensee MDPI, Basel, Switzerland. This article is an open access article distributed under the terms and conditions of the Creative Commons Attribution (CC BY) license (<https://creativecommons.org/licenses/by/4.0/>).

1. Introduction

Global warming is exacerbated by the significant carbon dioxide emissions of extensive fossil fuel use [1]. Governments worldwide have enacted the Paris Agreement to mitigate climate change, aiming to limit global warming to 1.5 °C above pre-industrial levels [2]. Transportation electrification is one of the main pathways to achieving the Paris Agreement. To improve energy efficiency, the multiport energy management system (EMS) has been researched and applied in several areas of transportation electrification, including hybrid electric vehicles and hybrid electric vessels [3,4].

The multiport EMS generally connects lithium batteries, supercapacitors, diesel generators, and electric motors through DC buses [5]. The batteries and supercapacitors are usually integrated to form a hybrid energy storage system (ESS). The ESS can drive the electric motors and supply power to other electrical equipment. It can be powered by the auxiliary power unit [6,7], which is very important as it extends the range of the vehicles or vessels. Therefore, the multiport EMS has a hybrid electric power supply system. Compared with the low efficiency of conventional diesel propulsion systems, the hybrid electric power supply system exhibits dual efficiency and stability advantages when applied to hybrid vehicles or vessels [5,8–11].

To achieve high energy efficiency, efficient EMS control strategies and optimization methods need to be investigated, such as rule-based [12–14] and fuzzy logic [15,16] control methods, genetic algorithms [17,18], and neural networks [19,20]. The rule-based EMS

control strategy is the most effective method for commercial range-extended systems [7]. However, the design of the rules requires rich engineering experience, mathematical models, and extensive data [21]. Despite the wide application of rule-based energy management strategies in range-extended EMS, there are still opportunities for fuel and energy efficiency enhancements [22,23].

In addition to energy efficiency, several other challenges exist for developing an efficient EMS for (range-extended) hybrid electric vessels. First, the peak discharge current can significantly reduce lithium batteries' lifespan. Second, the ESS with lithium batteries only struggles to meet the high transient power demand of the modern motors in vessels [24–26]. Although integrating supercapacitors can resolve these issues, this solution imposes higher requirements on the EMS control strategy and the ESS size [27]. The lithium battery should maintain within the optimal state of charge (SoC) range during operation. Insufficient SoC level will significantly reduce lithium battery efficiency and life span [28,29]. Predicted operational conditions might differ from actual conditions in SoC levels, potentially leading to SoC imbalance risks [30].

In this study, a multiport EMS was designed and modelled for a 150 kW range-extended towing vessel (RETV) by using MATLAB/Simulink. The multiport EMS included a diesel generator system, a drive system with a permanent magnet synchronous motor (PMSM) and its controller, a lithium battery, and supercapacitors. A typical operation cycle with five operation conditions was proposed for the investigated 150 kW RETV in terms of power demand. Then, a rule-based expert control strategy was proposed to control the EMS to improve the overall energy efficiency of the RETV. Experimental scenarios were designed to verify whether the proposed multiport EMS enables the RETV to balance fuel economy and battery life, and reduce the high current impact. The main contributions of this work are as follows.

- Define five typical operating conditions for a 150 kW RETV regarding the energy flow and power demand.
- Propose a rule-based expert control strategy, enabling the EMS to support various power demands.
- Construct the EMS simulation platform for the 150 kW RETV by incorporating the proposed rule-based expert control strategy.

The remainder of this paper is organized as follows. Section 2 introduces the components and their models for the investigated 150 kW RETV. Section 3 details the RETV operating conditions for an operation cycle and the proposed rule-based expert control strategy. Section 4 details the simulation of the multiport EMS to verify the proposed expert control strategy, followed by the conclusion.

2. EMS Model for RETV

Figure 1 depicts the multiport EMS topology for the 150 kW RETV. In the topology, the diesel generator system was the primary power source to supply the RETV. The rest included a PMSM, a battery, and supercapacitors. The battery and supercapacitors were combined as the ESS. The diesel generator's output was rectified (by a rectifier) and connected to the ESS through the DC bus, and it was then supplied to the PMSM.

The models of the components are described in the following subsections.

2.1. Diesel Generator System Model

The output of the diesel generator was converted to DC via a three-phase controlled bridge-type rectifier, which then supplied the PMSM through the DC bus. The three-phase controlled bridge rectifier has wide application in medium- and high-power scenarios due to its small output voltage ripple, high pulse frequency, high-side power factor, and fast dynamic response [31]. As shown in Figure 2, the rectifier consisted of a common cathode group (VT_1 , VT_3 , and VT_5) and a common anode group (VT_2 , VT_4 , and VT_6). A three-phase Phase-Locked Loop (PLL) was integrated to ensure synchronization between

the rectifier and the diesel generator [31]. The parameters of the diesel generator system and three-phase PLL are listed in Table 1.

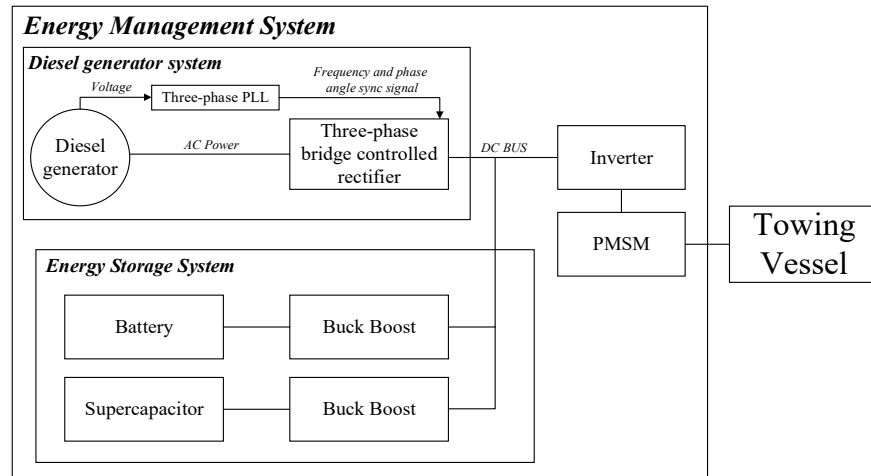


Figure 1. The proposed EMS for a 150 kW RETV.

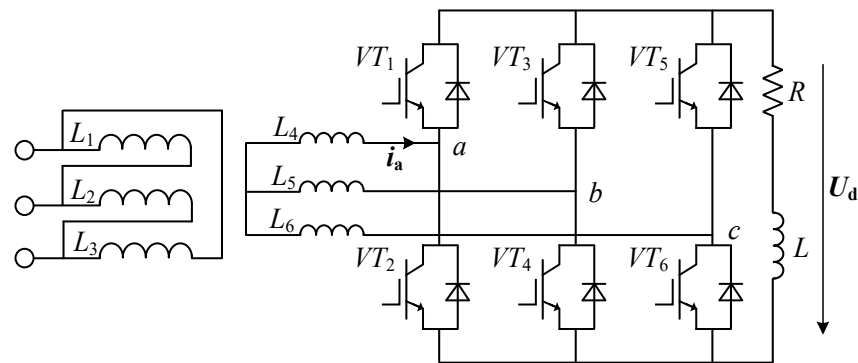


Figure 2. Circuit topology of a three-phase controlled bridge-type rectifier.

Table 1. Parameters of the diesel generator system and three-phase PLL.

Parameters	Value
PLL minimum frequency	45 Hz
PLL initial phase angle	0 degree
PLL initial frequency	50 Hz
Diesel generator system configuration	Yg
Diesel generator system three-phase voltage	380 V
Diesel generator system frequency	50 Hz
Diesel generator system initial phase angle	0 degree

2.2. ESS Model

2.2.1. Lithium Battery Model

The charging and discharging process of the lithium battery involves complex electrochemical reactions [32]. This study adopted the equivalent circuit model to describe the battery’s characteristics [33,34]. It used an internal resistance model to explain the battery’s charge and discharge processes.

Discharge ($i > 0$):

$$f_1(it, i^*, i, Exp) = E_0 - K \cdot \frac{Q}{Q - it} \cdot i^* - K \cdot \frac{Q}{Q - it} \cdot it + Laplace^{-1} \left(\frac{Exp(s)}{Sel(s)} \cdot 0 \right) \quad (1)$$

Charge ($i < 0$):

$$f_2(it, i^*, i, Exp) = E_0 - K \cdot \frac{Q}{Q - it} \cdot i^* - K \cdot \frac{Q}{Q - it} \cdot it + Laplace^{-1} \left(\frac{Exp(s)}{Sel(s)} \cdot \frac{1}{s} \right) \quad (2)$$

where

- E_0 is the battery's constant voltage;
- $Exp(s)$ is the battery's exponential area characteristic;
- K is the battery's polarity constant;
- i^* is the battery's low-frequency current characteristics;
- it is the battery's extraction capacity;
- Q is the battery's maximum battery capacity.

2.2.2. Supercapacitor Model

In this study, the carbon-based electric double-layer supercapacitors were chosen to form the EMS for the investigated RETV. Due to its safety, maturity, and cost-effectiveness, carbon-based electric double-layer supercapacitors are widely used in practical engineering applications [35]. The first-order RC model was been selected to represent it in this study. The output voltage of the supercapacitor can be expressed as

$$V_{SC} = \frac{N_s Q_T d}{N_p N_e \epsilon \epsilon_0 A_i} + \frac{2 N_e N_s R T}{F} \sinh^{-1} \left(\frac{Q_T}{N_p N_e^2 A_i \sqrt{8 R T \epsilon \epsilon_0 c}} \right) - R_{SC} \cdot i_{SC} \quad (3)$$

$$Q_T = \int i_{SC} dt \quad (4)$$

where

- A_i is the cross-sectional area of the electrode and electrolyte of the supercapacitor;
- c is the supercapacitor molar concentration;
- r is the supercapacitor molecular radius;
- F is the Faraday constant;
- i_{SC} is the supercapacitor current;
- V_{SC} is the supercapacitor voltage;
- R_{SC} is the supercapacitor resistance;
- N_e is the electrode layers;
- N_A is the Avogadro constant;
- N_p is the number of supercapacitors connected in parallel;
- N_s is the total resistance of the number of supercapacitors in series;
- Q_T is the charge;
- R is the ideal gas constant;
- d is the molecular radius;
- T is the operating temperature;
- ϵ is the permittivity of the material;
- ϵ_0 is the permittivity of free space.

The parameters of the proposed ESS are listed in Table 2.

2.2.3. Bidirectional Buck–Boost Converter Model

The bidirectional DC–DC converter is the conversion device between DC voltages. As shown in Figure 3, it can enable bidirectional energy transfer while maintaining the voltage polarity on both the input and output sides.

A non-isolated bidirectional buck–boost DC–DC converter was employed for the multiport EMS. This type of converter facilitates bidirectional power flow and voltage adjustment catering to ESS [36]. The non-isolated DC–DC converter had a simple structure and a small volume because there was no isolation transformer. It can realize highly efficient bidirectional power conversion in the ESS composed of battery and supercapacitors [37,38].

Table 2. Parameters of the ESS.

Parameters	Value
Lithium battery’s nominal voltage	600 V
Lithium battery’s rated capacity	1000 Ah
Lithium battery’s initial state of charge	75%/15%
Supercapacitors’ rated capacitance	700 F
Supercapacitors’ rated voltage	700 V
Supercapacitors’ initial state of charge	100%
Supercapacitors’ number of series capacitors	200
Supercapacitors’ number of parallel capacitors	5

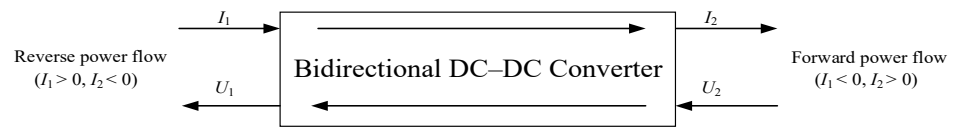


Figure 3. Energy flow diagram for a bidirectional DC–DC converter.

According to the current flow directions, the converter mainly worked in buck and boost modes. As shown in Figure 4, the U_1 was connected to the lithium battery that supplied power to the external load. The load was connected in parallel with the output capacitor C_2 , and the positive pole of the output voltage U_2 was downward. In this case, S_1 was the main switching tube and S_2 was the synchronous switching tube. Assuming D_1 is the duty cycle of S_1 , $T = 1/f_s$ is the switching period, where f_s is the switching frequency, and L is the inductance of the inductor L_1 .

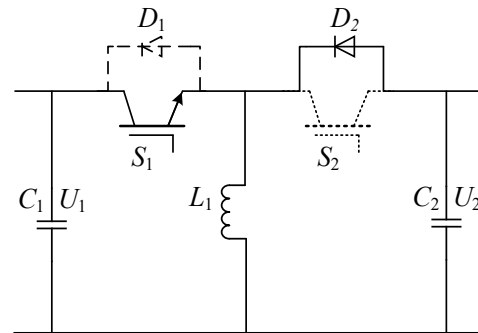


Figure 4. An equivalent circuit of the bidirectional DC–DC buck–boost converter in the boost mode.

The working principle of the boost mode can be explained as follows.

First, when $0 < t < D_1T$, the switch S_1 is turned on, and the switch S_2 is turned off. The inductor voltage $U_L = U_1$, and the inductor current is

$$i_L(t) = \frac{1}{L} \int_0^t U_L dt + i_L(0) = \frac{U_L}{L} t + i_L(0) \tag{5}$$

Bringing $t = D_1T$ into the Equation (6), the peak value of the AC component of the inductor current is obtained as

$$\Delta i_L = i_L(D_1T) - i_L(0) = \frac{U_L D_1}{f_s L} \tag{6}$$

where the drain-source voltage is 0 for the switch S_1 ($U_{DS1} = 0$), the drain-source current is I_L ($I_{D1} = I_L$), the drain-source voltage is $U_1 + U_2$ for the switch S_2 ($U_{DS2} = U_1 + U_2$), and the drain-source current is 0 ($I_{D2} = 0$).

Second, when $D_1T < t < T$, the switch S_1 is turned off and S_2 is turned on. The inductor voltage $U_L = -U_2$, and the inductor current is

$$i_L(t) = -\frac{U_2}{L}(t - D_1T) + i_L(D_1T) \tag{7}$$

Other relevant voltages and current values are as follows.

$$\Delta i_L = i_L(D_1T) - i_L(0) = \frac{U_2(1 - D_1)}{f_s L} \tag{8}$$

$$U_{DS1} = U_1 + U_2, I_{D1} = 0, U_{DS2} = 0, I_{D2} = I_L$$

The ideal DC voltage conversion ratio in the discharge state is

$$M_U = \frac{U_2}{U_1} = \frac{D_1}{1 - D_1} \tag{9}$$

Figure 5 shows an equivalent circuit diagram for the bidirectional DC–DC buck–boost converter in buck mode. As shown, S_2 was the main switch, S_1 was used as the synchronous switch, and D_2 was the duty ratio of S_2 . U_2 charged the lithium battery pack in this case.

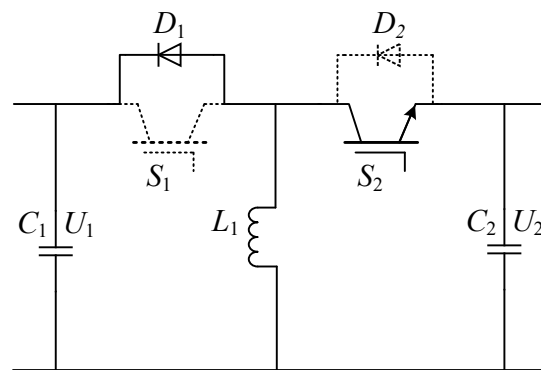


Figure 5. An equivalent circuit diagram for the bidirectional DC–DC buck–boost converter in buck mode.

Third, when $0 < t < D_2T$, switch S_2 is turned on and S_1 is turned off. The inductor voltage $U_L = U_2$, and the inductor current is

$$i_L(t) = \frac{U_2}{L}t + i_L(0) \tag{10}$$

Bringing $t = D_2T$ into Equation (11), the peak-to-peak value of the AC component of the inductor current is obtained as

$$\Delta i_L = \frac{U_L D_2}{f_s L} \tag{11}$$

where the drain-source voltage is 0 ($U_{DS2} = 0$) for the switch S_2 , the drain-source current is $I_{D2} = I_L$, the drain-source voltage is $U_{DS1} = U_1 + U_2$ for the switch S_1 , and the drain-source current is $I_{D1} = 0$.

Finally, when $D_2T < t < T$, the switch S_2 is turned off and S_1 is turned on. The inductor voltage $U_L = -U_1$, and the inductor current is

$$i_L(t) = -\frac{U_1}{L}(t - D_2T) + i_L(D_2T) \tag{12}$$

Other relevant voltages and current values are as follows.

$$\Delta i_L = i_L(D_2T) - i_L(0) = \frac{U_1(1 - D_2)}{f_s L} \tag{13}$$

$$U_{DS2} = U_1 + U_2, I_{D2} = 0, U_{DS1} = 0, I_{D1} = I_L$$

The ideal DC voltage conversion ratio in the charge state is

$$M_U = \frac{U_1}{U_2} = \frac{D_2}{1 - D_2}. \tag{14}$$

The control strategy for the bidirectional DC–DC converter was based on EMS power distribution. For example, when the converter works in the discharge mode, a discharge current should be output and maintained by Proportional Integral (PI) controllers. The overall control logic is shown in Figure 6. The parameters for the bidirectional DC–DC buck–boost converter are tabulated in Table 3.

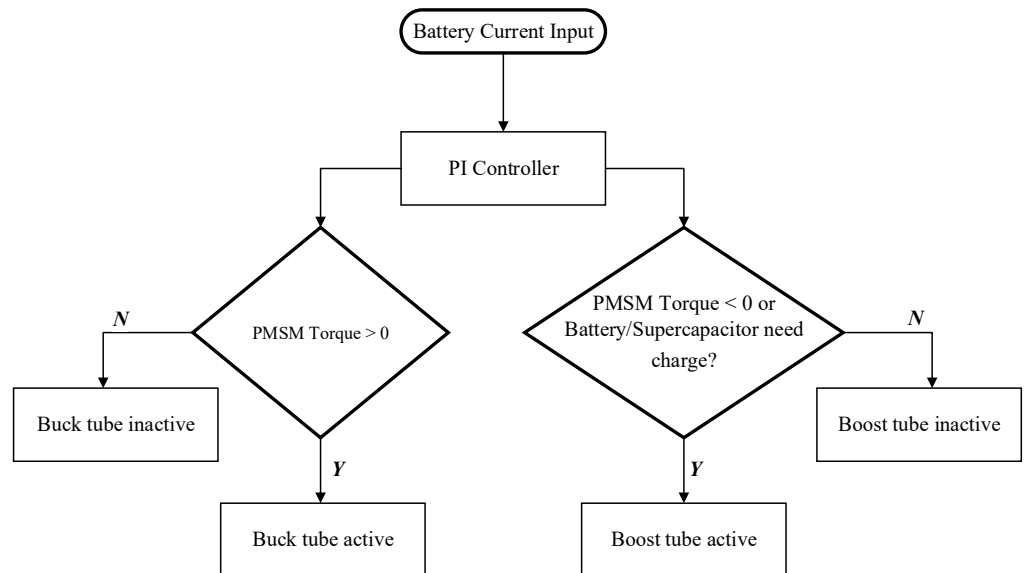


Figure 6. The control logic of the bidirectional DC–DC buck–boost converter.

Table 3. Parameters of the bidirectional DC–DC buck–boost converter.

Parameters	Value
Converter internal resistance	$1 \times 10^{-3} \Omega$
Converter snubber resistance	$1 \times 10^5 \Omega$
Converter snubber capacitance	inf
Proportional factor of lithium battery PI controller	0.1
Integral factor of lithium battery PI controller	0.05
Proportional factor of supercapacitors PI controller	0.3
Integral factor of supercapacitors PI controller	0.02

2.3. PMSM Control Model

PMSMs have gained popularity in marine propulsion due to their high efficiency and power density [39,40]. PMSMs leverage vector control for efficient operation. Implementing this control technique involves transitioning from a three-phase system (*abc*) to a two-phase quadrature system (*dq*), to state the mathematical models of PMSMs [41,42]. Figure 7 shows a block diagram for the vector control of PMSMs. Three PI controllers were used to achieve speed and current adjustment. Their parameters are listed in Table 4.

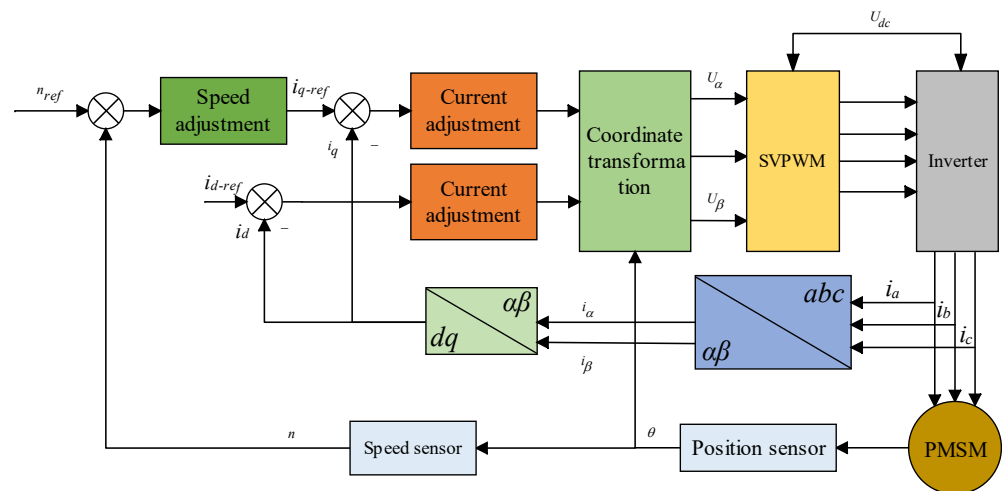


Figure 7. A block diagram for the vector control of PMSMs.

Table 4. Parameters of the PI controller for vector control of PMSMs.

Parameters	Value
Speed loop P	0.2
Speed loop I	100
Speed loop saturation	−3000, 3000
q axis current loop proportional factor	40
q axis current loop integral factor	50
q axis current loop saturation	−500, 500
d axis current loop proportional factor	20
d axis current loop integral factor	5
d axis current loop saturation	−500, 500

3. Rule-Based Expert Control Strategy for the EMS of RETV

The EMS manages the power distribution between the ESS and the diesel generator system during operation, aiming to maximize the benefits of the lithium battery and supercapacitors. The rule-based expert control strategy was formulated to adjust the lithium battery’s discharge process. This strategy reduces the high current impact on the lithium battery, compensates for sudden power demands with supercapacitors, and maintains the ESS in optimal condition during charging and discharging cycles.

3.1. Statement of 150 kW RETV Operation Conditions

A typical driving cycle of the RETV can have five operation stages: start-up, before cruise, cruise, towing, and end towing. The details are explained as follows.

3.1.1. Start-Up

At this stage, the RETV requires a large power demand, and the lithium battery is the primary power source. Supercapacitors are the backup power source to balance the increased power demand and reduce lithium battery loss. Charging is processed depending on the SoC level. The energy flow of the start-up process is shown in Figure 8.

3.1.2. Before Cruise

The RETV operates at a fixed speed (lower than the peak speed) before the cruise as it normally waits for future instructions after start-up. The battery drives the RETV to the required speed at this stage. The diesel generator system does not contribute due to low power efficiency in this condition. The supercapacitors do not work because there is no sudden power change. Charging may occur depending on the SoC level. The energy flow of the EMS before the cruise stage is shown in Figure 9.

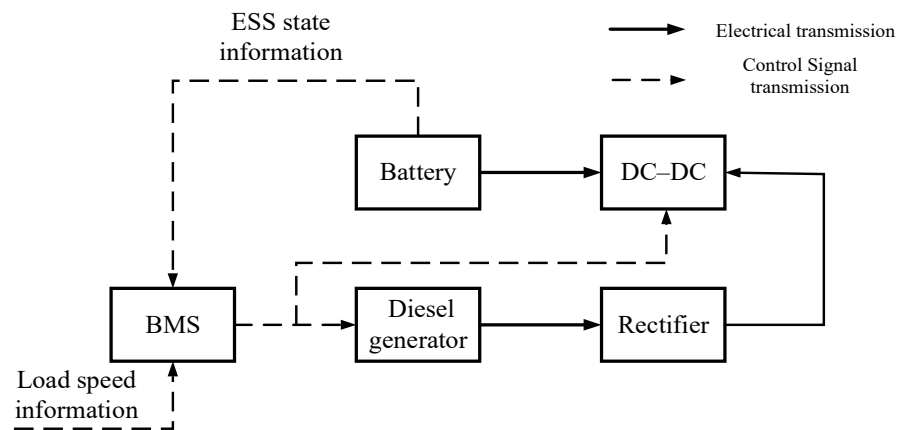


Figure 8. Energy flow of the EMS under start-up stage.

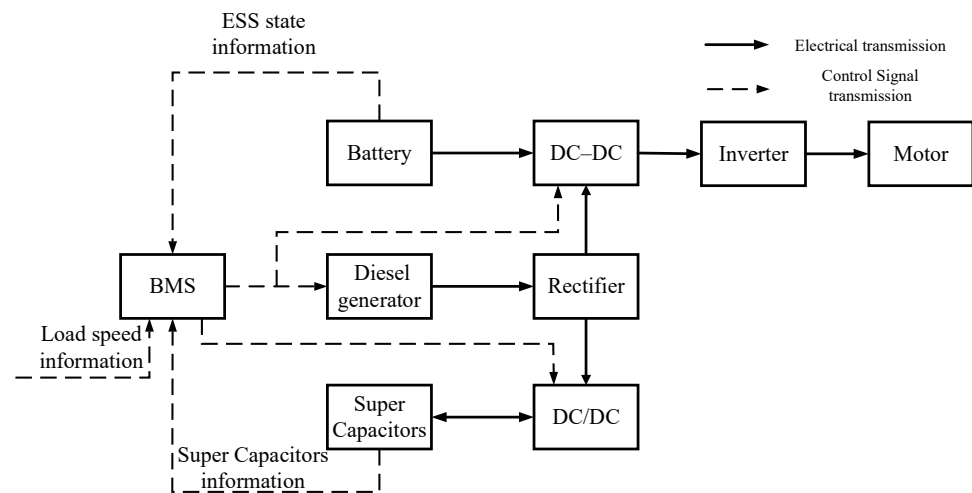


Figure 9. Energy flow of the EMS at the stage before cruise.

3.1.3. Cruise

In the cruise stage, the RETV reaches and maintains peak speed with rated power. The diesel generator system is active at this stage as it can provide constant power at high speed [43–45]. When the operating speed exceeds 87% of its peak rotating speed, the RETV is regarded as working in the cruise stage. Since the battery performs poorly when discharging in the high-power demand period, the diesel generator system directly drives the PMSM alone [46,47]. Supercapacitors address sudden power demand while transitioning to peak speed with rated power. The battery and supercapacitors may be charged due to their SoC levels. The energy flow of the EMS under cruise is shown in Figure 10.

3.1.4. Towing

When the RETV is towing, its cruising speed is reduced compared with the peak speed. Due to the reduced power demand, the lithium battery is the energy source. The lithium battery and supercapacitors may be charged due to their SoC levels. The energy flow of the EMS under towing is shown in Figure 11.

3.1.5. End Towing

At this stage, the rotor speed will be higher than the synchronous speed, and the generated reverse power charges the battery and supercapacitors. The energy flow of the EMS under end towing is shown in Figure 12.

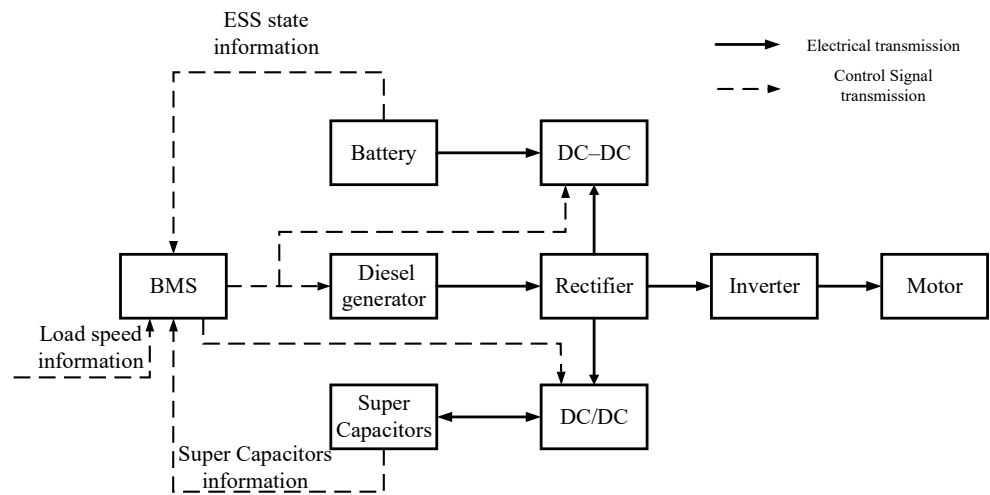


Figure 10. Energy flow of the EMS under cruise operation.

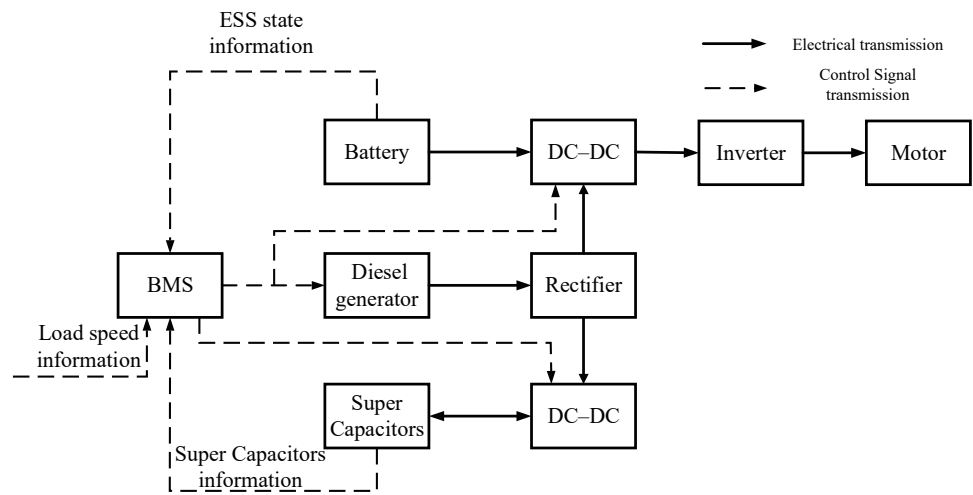


Figure 11. Energy flow of the EMS under towing operation.

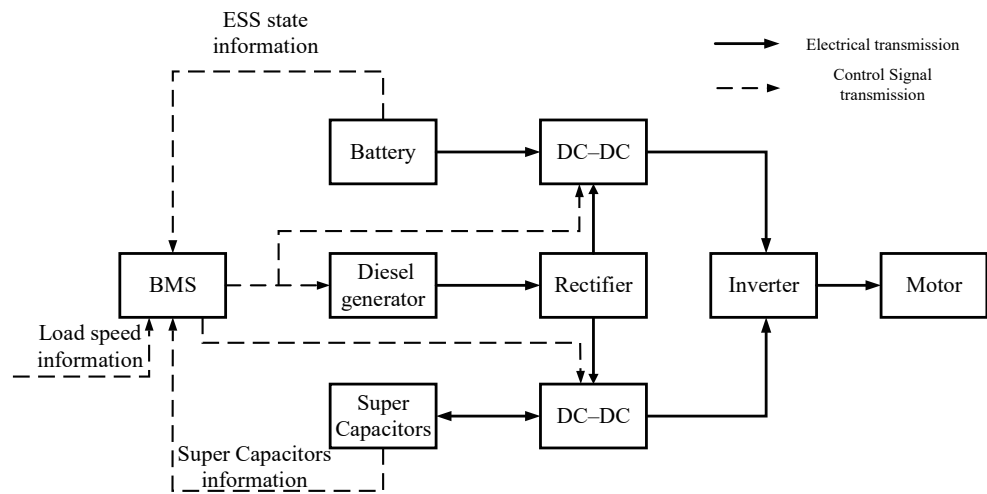


Figure 12. Energy flow of the EMS under end towing operation.

3.2. Expert Control Strategy for the EMS

The EMS control target is to distribute power between the ESS and the diesel generator system. By monitoring the SoC level of the ESS, charging can be dynamically adjusted to

meet the PMSM’s power demands. As the ESS design combines the battery and supercapacitors, the EMS’s rule-based expert control strategy is complex, as each component can be either charged or discharged.

The operating conditions of the RETV are relatively fixed, making it suitable for the rule-based expert control strategy. The logical threshold control decomposes the RETV’s different operation stages into control parameters, providing a tailored control strategy for each stage to ensure comprehensive energy management.

According to the analysis of the operation stages, we set the PMSM power demand P_t , and lithium battery SoC_b as the threshold values. Operating the lithium battery at low SoC accelerates aging. To optimize the battery’s lifespan, we set the upper and lower thresholds of SoC_b as 0.9 (SoC_{bMAX}) and 0.2 (SoC_{bMIN}), respectively. When P_t was greater than the rated output power of the battery, the diesel generator system was used as the compensation power supply to supply the extra power demand. The control logic flowchart is shown in Figure 13. The specific rules were as follows:

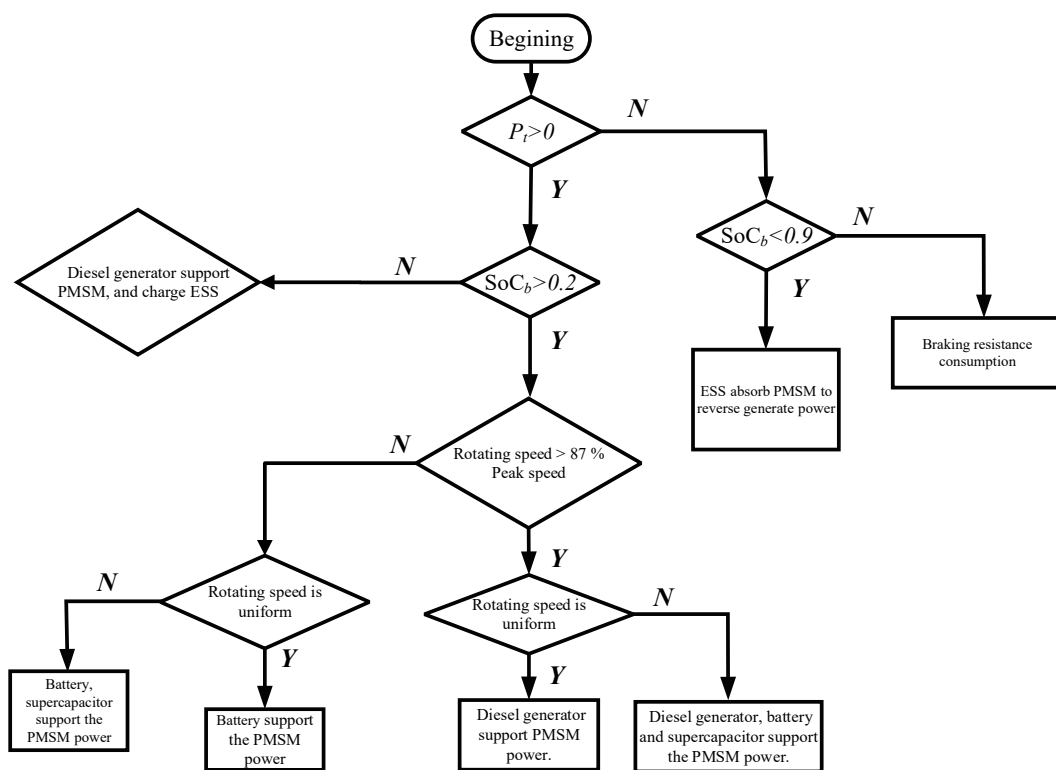


Figure 13. A schematic diagram for the expert control strategy of EMS for the RETV.

1. When $P_t > 0$ and $SoC_b > SoC_{bMIN}$
 If the rotating speed of the PMSM was not fixed in the high-speed range (beyond 87% of its peak speed), the lithium battery and supercapacitors could supply the RETV. If the rotating speed was fixed in the high-speed range, the diesel generator system supplied the PMSM. If the rotating speed of the PMSM was not fixed and was less than 87% of its peak speed, the lithium battery and supercapacitors supplied the RETV for various power demands. If the rotating speed was fixed and was less than 87% of its peak speed, only the lithium battery supported the RETV.
2. When $P_t > 0$ and $SoC_b < SoC_{bMIN}$
 As the lithium battery and supercapacitors could not supply the RETV in this operation stage, the diesel generator system joined in and compensated for power. The lithium battery and supercapacitors were charged if necessary.

3. When $P_t < 0$ and $\text{SoC}_b < \text{SoC}_{bMAX}$
The RETV worked under the end towing stage. The PMSM acted as a reverse power generator. The lithium battery and supercapacitors were charged in this case.
4. When $P_t < 0$ and $\text{SoC}_b > \text{SoC}_{bMAX}$
The braking resistor consumed the negative power.

3.3. The Analysis of PMSM Reverse Generation

When the PMSM rotor rotated in the same direction, the rotor speed exceeded the stator magnetic field speed due to inertia, which resulted in the PMSM entering a regenerative power generation state. The power generated by the asynchronous PMSM was returned to the DC link of the inverter through the six freewheeling diodes of the inverter (IGBT). Reverse power generation in the RETV occurred at the end of towing. Large inertia retained from descending from higher speeds caused the rotor to rotate faster than its synchronous speed. Additionally, the water resistance and external torque generated by the physically connected towing object contributed to this phenomenon.

3.4. PMSM Load Design

The RETV's power demand was calculated based on different operation stages. The calculated power demand was the product of the PMSM speed and torque, as shown in Table 5. To shorten the simulation time, the time of an operation cycle was set at 20 s. The reference speed and torque demand of the PMSM are shown in Figures 14 and 15, respectively.

Table 5. PMSM speed and torque demand value sheet.

Time (s)	RPM (r/min)	Torque (Nm)
0	0	0
1	0	0
1.25	42	218
1.50	85	437
2.00	170	873
3.00	340	1747
4.00	416	2800
5.00	416	2800
6.00	416	2800
7.00	478	3000
8.00	478	3000
9.00	478	3000
10.00	478	3000
10.50	424	2750
11.00	370	2500
12.00	370	2500
13.00	370	2500
14.00	370	2500
15.00	210	0
16.00	50	−2500
17.00	50	−2500
18.00	50	−2500
19.00	50	−2500
19.50	25	−2500

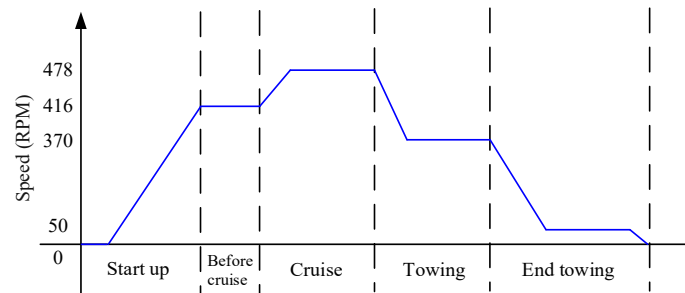


Figure 14. PMSM speed demand for the five operation conditions.

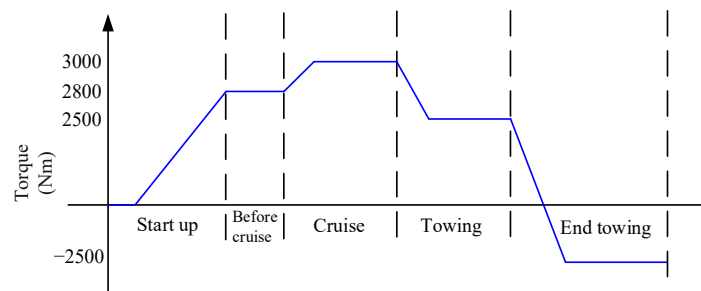


Figure 15. PMSM torque demand for the five operation conditions.

4. Simulation

4.1. PMSM Load Simulation

PMSM speed and torque demands were simulated over an operation cycle. The powergui was set as Discrete with a sampling time of 1×10^{-5} in Matlab/Simulink. Due to the static resistance (viscous resistance or frictional resistance) generated by the relative movement of the RETV and the sea surface, additional energy was consumed to resist the irregular motion of the sea-surface waves. The PMSM power fluctuations were limited to within 5%. The units for the PMSM speed, torque, and power were set as rad/s, Nm, and kW, respectively, to unify and clearly show the results. The results depicted in Figures 16 and 17 illustrate the comparison between the designed and simulated speed, torque, and power. These figures demonstrate that the PMSM load simulations are consistent with engineering reality.

4.2. Simulation of ESS

Three case studies, as shown below, were simulated and analyzed for the ESS.

- Case 1: ESS with a satisfied initial battery condition (75% SoC).
- Case 2: ESS with the lithium battery only and satisfied initial battery condition (75% SoC).
- Case 3: ESS with an unsatisfied initial battery condition (15% SoC).

4.2.1. Case 1: ESS with a Satisfied Initial Battery Condition (75% SoC)

Figure 18a shows the required output power of the PMSM (P_{PMSM}) and the power provided by the battery (P_{LB}), supercapacitors (P_{SC}), and diesel generator (P_{EG}) by using the proposed EMS in this case. In the simulation, the battery's initial SoC was set as 75%. Table 6 lists the power data for nine operating points at different times. The following analysis was conducted.

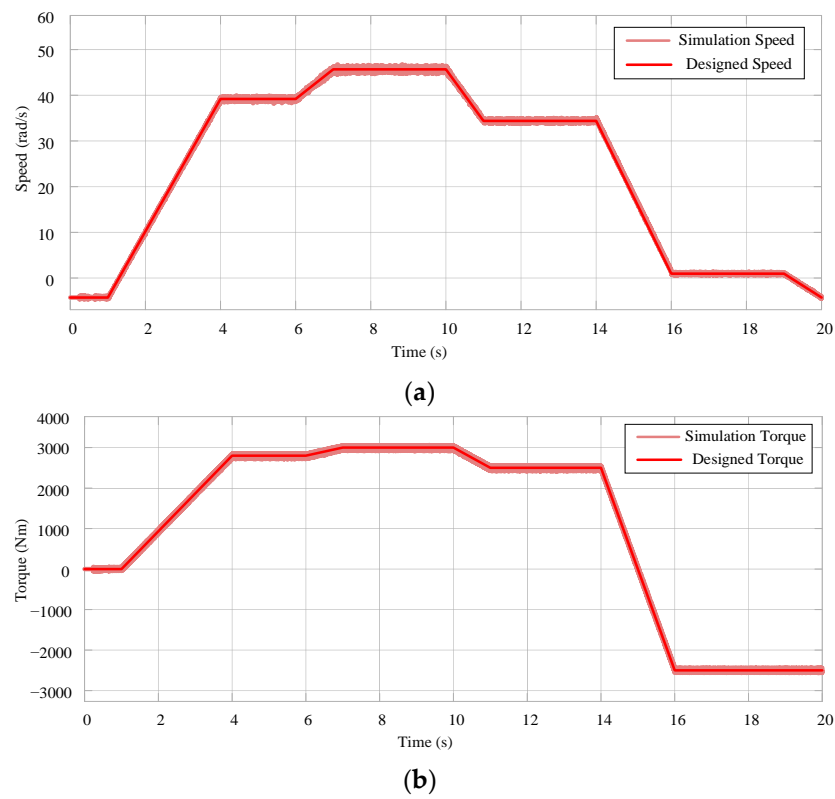


Figure 16. The designed and simulated response of (a) PMSM speed, and (b) torque.

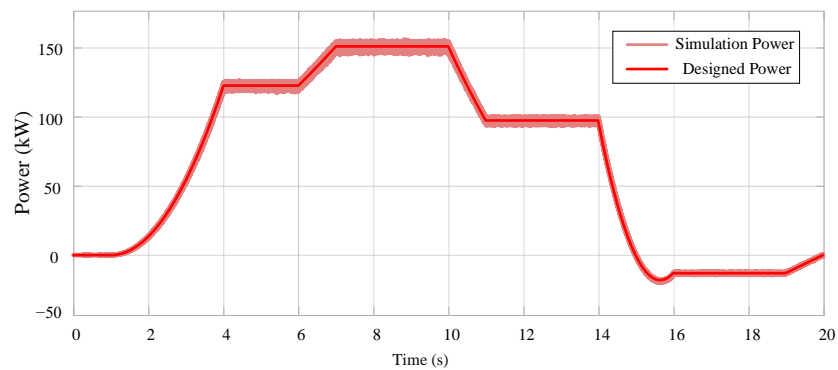


Figure 17. The designed and simulated response of the output power of the PMSM.

Table 6. Power data for case 1.

Time (s)	P_{LB} (kW)	P_{SC} (kW)	P_{EG} (kW)	P_{PMSM} (kW)
0	0	0	0	0
1	0	0	0	0
3	30	20	0	50
4	120	0	0	120
7	0	0	150	150
10.5	77	0	43	120
11	100	0	0	100
15	100	0	0	100
16	-13.3	0	0	-13.3

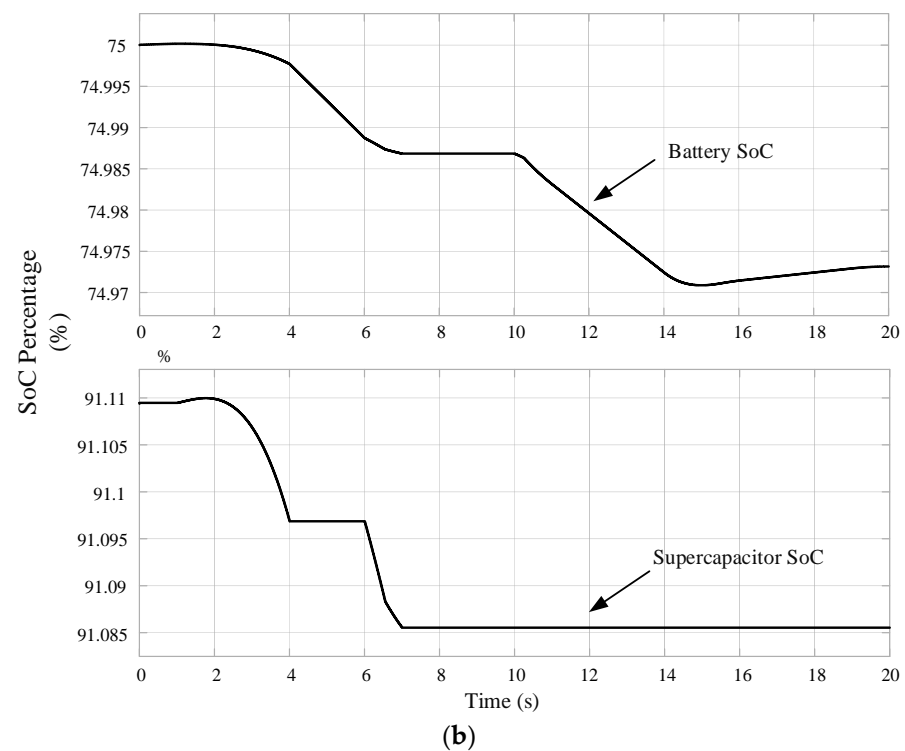
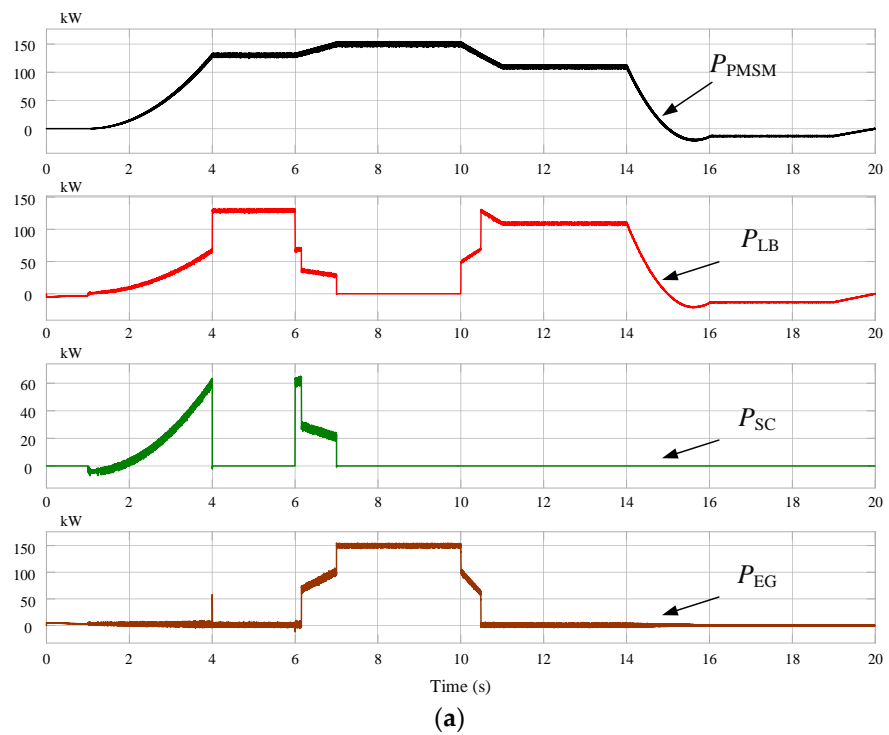


Figure 18. (a) EMS power curves for case 1; (b) SoC curves of the battery and supercapacitors for case 1.

- (1) During the start up stage (0–4 s), the ESS supplied the PMSM’s power demand. Both P_{LB} and P_{SC} reached up to 60 kW.
- (2) Between 4–6 s, the RETV entered the before-cruise stage. The lithium battery powered the RETV with about 120 kW. The P_{SC} and P_{EG} remained at 0 W.
- (3) During cruise (6–10 s), the PMSM power demand initially rose, then stabilized. The supercapacitors assisted the lithium battery in meeting the surge in power demand.

The diesel generator system output ramped up to 100 kW between 6–7 s, ultimately supplying 150 kW when cruising at peak speed.

- (4) In towing (10–14 s), the PMSM required a lower constant power, around 100 kW, provided by the lithium battery. The P_{SC} and P_{EG} remained at 0 W.
- (5) From 14 s to 20 s, the lithium battery was charged due to the reversal of the PMSM. It stabilized at 13.3 kW at 16 s.
- (6) Table 6 demonstrates the power demand successfully distributed by the EMS throughout one operation cycle. The PMSM-demanded power for one operation cycle was 0.3942 kWh, and the diesel generator system and ESS output power was 0.4415 kWh. The comprehensive energy efficiency of the EMS was approximately 85%.

Figure 18b shows the SoC curves of the lithium battery and supercapacitors in case 1. As shown, the ESS provided the power demand during start-up, so the SoC of the lithium battery was reduced during 0–6 s. The SoC of the supercapacitors also had a certain decrease during the first operation stage (0–4 s). After that, the lithium battery provided power as the operation stage switched to towing, causing the SoC of the lithium battery to drop to 74.97%. The SoC gradually increased due to reverse charging from the PMSM.

4.2.2. Case 2: ESS with the Lithium Battery Only and Satisfied Initial Battery Condition (75% SoC)

This case study compared the performance of the EMS with and without supercapacitors to show the advantages of using supercapacitors in the ESS. In this study, the capacitors were mainly used to address the sudden power demand and large discharge current. For this purpose, the results for two simulation periods (3.995–4 s and 6.837–6.841 s) were investigated. Figures 19 and 20 show the battery's discharge current waveforms and SoC curves of the two ESS systems, respectively. Please note that the hybrid ESS shown in the two figures means the ESS with both battery and supercapacitors. The following analysis was conducted:

- (1) In the period 3.995–4 s, the ESS with lithium battery only maintained a peak current of about 190 A, which was 1.9 times higher than that of the hybrid ESS (100 A).
- (2) In the period of 6.837–6.841 s, the ESS with lithium battery only maintained a peak current of about 85 A, which was 1.7 times higher than that of the hybrid ESS (50 A).
- (3) The SoC decrease rate for the ESS with lithium battery only was faster than that of the hybrid ESS before 4 s. At 4 s, the battery's SoC of the ESS with lithium battery only dropped to 74.996%, which was slightly lower than that of the hybrid ESS (74.998%).
- (4) Both systems showed a consistent SoC decrease rate during 4–6 s. In the subsequent cruise, the sudden power demand decreased the battery's SoC. At 7 s, the battery's SoC of the ESS with lithium battery only fell to 74.985%, which was also lower than that of the hybrid ESS (74.988%).

Therefore, the hybrid ESS outperformed the ESS with lithium battery only in reducing the impact of sudden power demands. This indicates that the hybrid ESS has a smaller energy flow in the lithium battery. It can also be seen from the SoC curves that the energy consumed by the hybrid ESS was lower than that of the ESS with lithium battery only. It proved that the supercapacitors in the hybrid ESS allowed the battery to discharge more stably and avoided the impact of the high discharge current, so as to reduce the battery's aging rate.

4.2.3. Case 3: ESS with an Unsatisfied Initial Battery Condition (15% SoC)

In this case, the initial SoC of the battery was set as 15%. According to the power demand of the PMSM, the output power of the lithium battery, supercapacitors, and diesel generator system is shown in Figure 21a. The power data for several typical operation points are listed in Table 7. The following analysis was conducted:

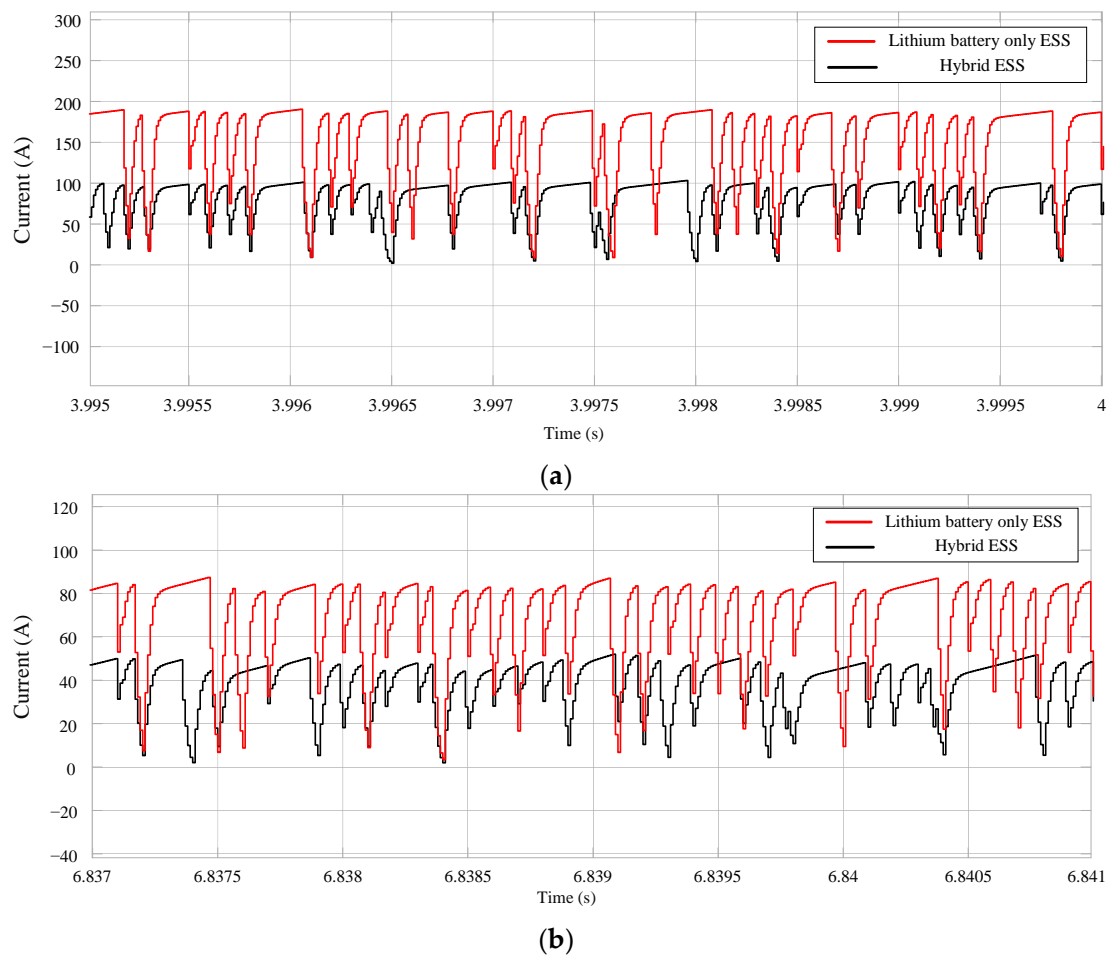


Figure 19. Battery discharge current for two ESS systems: (a) simulation period, 3.995–4 s; and (b) simulation period, 6.837–6.841 s.

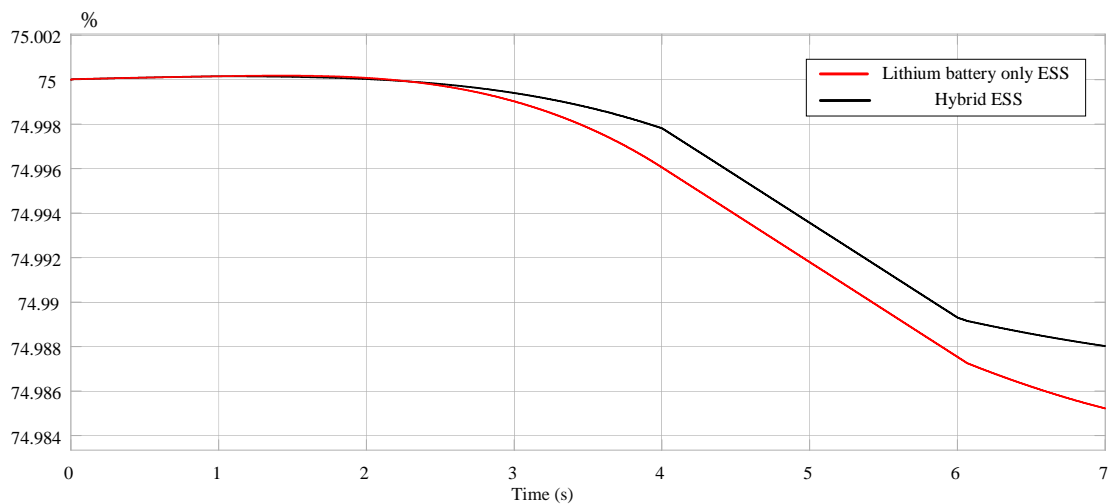


Figure 20. SoC curves for two ESS systems.

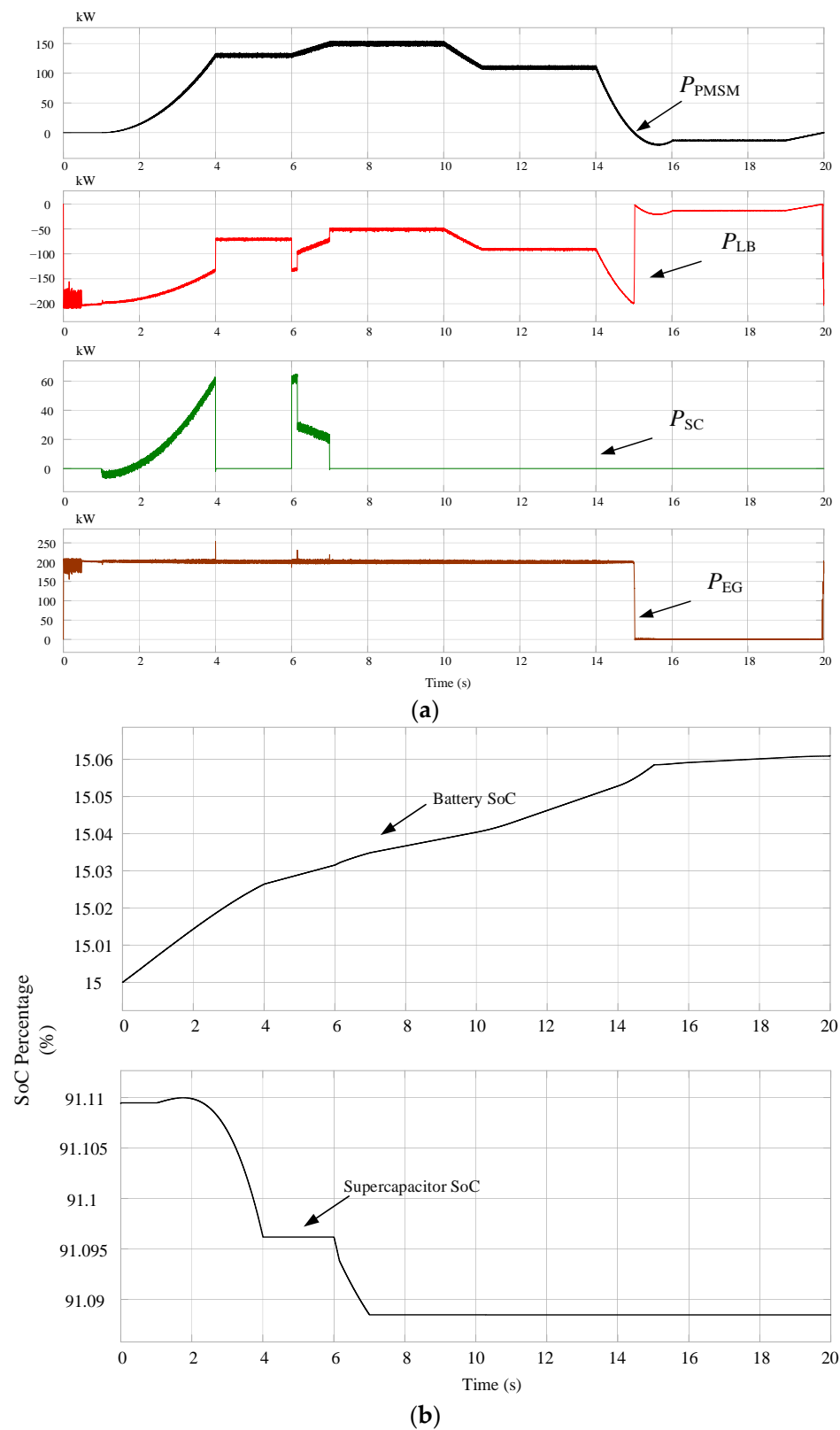


Figure 21. (a) EMS power curves for case 3; (b) SoC curves of the battery and supercapacitors for case 1.

Table 7. Power data for case 3.

Time (s)	P_{LB} (kW)	P_{SC} (kW)	P_{EG} (kW)	P_{PMSM} (kW)
0	0	0	0	0
1	0	0	0	0
3	−170	20	200	50
4	−80	0	200	120
7	−50	0	200	150
10.5	−80	0	200	120
11	−100	0	200	100
15	0	0	0	0
16	−13.3	0	0	−13.3

- (1) During the initial stage (0–4 s), the supercapacitors and the diesel generator system supplied the PMSM. The battery was charged as its SoC dropped below 20%. The charging power diminished from 200 kW to 80 kW due to the continuous rise of the PMSM power demand.
- (2) In the before-cruise stage, the diesel generator system provided the entire power demand, simultaneously providing consistent charging to the lithium battery during 4–6 s. The charging power to the lithium battery was constant at 80 kW. The diesel generator's output power was 200 kW.
- (3) During the cruise stage (6–10 s), the diesel generator system and supercapacitors supported the RETV until its speed peaks. After that, the diesel generator system contributed to the peak power demand (150 kW). The battery's charging rate declined when the power was around 50 kW.
- (4) As the power demand decreased during the towing stage (10–14 s), the charging power of the lithium battery increased to 100 kW. The diesel generator system provided a total of 200 kW, of which 100 kW went to the PMSM.
- (5) In the end towing stage (after 15 s), the lithium battery received a small amount of charging power, 13.3 kW, from the PMSM until the end of the operation cycle at 20 s.
- (6) As shown in Table 7, the power demand of the PMSM in one operation cycle was 0.3742 kWh, while the diesel generator system and ESS output power was 0.4418 kWh. The comprehensive energy efficiency of the EMS was approximately 85%.

Figure 21b shows the SoC curves of the battery and supercapacitors during an operation cycle. As shown, because the lithium battery SoC continued to be below the limit (20%), it remained charged for 0–20 s. At 0–4 s, it had the highest charging power due to the lower PMSM power demand. During the working stages, with constant speed, the diesel generator system provided uniform charging power, which can be explained by the stable increase in the SoC in 6–10 s. The reduced charging power after 15 s was provided by the reverse charging of the PMSM. The performance of the supercapacitors in this case was consistent with the performance in case 1.

5. Conclusions

This paper proposed a multiport EMS with a rule-based expert control strategy for a 150 kW RETV. Three case studies were conducted to show the effectiveness and advantages of the proposed EMS. The following conclusion can be drawn:

- (1) When the initial SoC of the battery is in the satisfactory range, like 75%, the proposed EMS can effectively distribute energy among the diesel generator system, lithium battery, and supercapacitors according to the requirements of each operation stage. The simulation results for two ESSs (with and without supercapacitors) showed that the hybrid ESSs have better performance when handling sudden power demand and big battery current.
- (2) When the initial SoC of the battery is not in the satisfactory range, like 15%, the system operates normally without the battery. It was found that the diesel generator system continuously charges the battery before the PMSM reverse charging occurs. The EMS

- showed the flexibility to maintain operational efficiency while the battery is less than ideal and extended the battery lifespan by keeping it within its optimal SoC range.
- (3) The simulation revealed that the comprehensive energy efficiency of the designed RETV is approximately 85% under the typical operation cycle proposed in this paper.

Author Contributions: Conceptualization, H.W.; methodology, H.W.; project administration, Y.Z.; software, Y.Z. and H.W.; supervision, G.L. and J.Z.; validation, Y.Z.; writing—original draft, Y.Z.; writing—review and editing, Y.Z., H.W. and Y.L. All authors have read and agreed to the published version of the manuscript.

Funding: This research received no external funding.

Institutional Review Board Statement: Not applicable.

Informed Consent Statement: Not applicable.

Data Availability Statement: Data are contained within the article.

Acknowledgments: We thank Gang Liu (Shenzhen SureTech Technology Co., Ltd., Shenzhen, China) for providing technical and software assistance, significantly supporting this research design and simulation.

Conflicts of Interest: The authors declare no conflict of interest.

Nomenclature

PMSM	Permanent Magnet Synchronous Motor
EMS	Energy Management System
ESS	Energy Storage System
EV	Electrical Vehicle
PI	Proportional Integral
RETV	Range-Extended Towing Vessel
SoC	State of Charge
2Level-VSI	Two-level inverter circuit
E_0	Battery constant voltage
$Exp(s)$	Battery exponential area characteristic
K	Battery polarity constant, V/Ah or polarity internal resistance
i^*	Battery low-frequency current characteristics
i	Battery current
it	Battery extraction capacity
Q	Battery maximum battery capacity
A_i	Supercapacitor cross-sectional area of electrode and electrolyte
c	Supercapacitor molar concentration
r	Supercapacitor molecular radius
F	Faraday constant
i_{SC}	Supercapacitor current
V_{SC}	Supercapacitor voltage
R_{SC}	Supercapacitor resistance
N_e	Electrode layers
N_A	Avogadro constant
N_p	Number of supercapacitors connected in parallel
N_S	The total resistance of the number of supercapacitors in series
N_e	Electrode layers
Q_T	Charge
R	Ideal gas constant
d	Molecular radius
T	Operation temperature
ε	Permittivity of the material
ε_0	Permittivity of free space

References

1. Harrouz, A.; Belatrache, D.; Boulal, K.; Colak, I.; Kayisli, K. Social Acceptance of Renewable Energy dedicated to Electric Production. In Proceedings of the 2020 9th International Conference on Renewable Energy Research and Application (ICRERA), Glasgow, UK, 27–30 September 2020; pp. 283–288.
2. UNFCCC. The Paris Agreement—Publication. In Proceedings of the Paris Climate Change Conference, Paris, France, 12 December 2015.
3. Hannan, M.A.; Hoque, M.M.; Hussain, A.; Yusof, Y.; Ker, P.J. State-of-the-Art and Energy Management System of Lithium-Ion Batteries in Electric Vehicle Applications: Issues and Recommendations. *IEEE Access* **2018**, *6*, 19362–19378. [[CrossRef](#)]
4. Schäfer, J.; Bortis, D.; Kolar, J.W. Multi-port multi-cell DC/DC converter topology for electric vehicle's power distribution networks. In Proceedings of the 2017 IEEE 18th Workshop on Control and Modeling for Power Electronics (COMPEL), Stanford, CA, USA, 9–12 July 2017; pp. 1–9.
5. Camara, M.B.; Payman, A.; Dakyo, B. Energy management based on frequency approach in an electrical hybrid boat. In Proceedings of the 2016 International Conference on Electrical Systems for Aircraft, Railway, Ship Propulsion and Road Vehicles & International Transportation Electrification Conference (ESARS-ITEC), Toulouse, France, 2–4 November 2016; pp. 1–6.
6. Emadi, A.; Lee, Y.J.; Rajashekara, K. Power Electronics and Motor Drives in Electric, Hybrid Electric, and Plug-In Hybrid Electric Vehicles. *IEEE Trans. Ind. Electron.* **2008**, *55*, 2237–2245. [[CrossRef](#)]
7. Xiao, B.; Ruan, J.; Yang, W.; Walker, P.D.; Zhang, N. A review of pivotal energy management strategies for extended range electric vehicles. *Renew. Sustain. Energy Rev.* **2021**, *149*, 111194. [[CrossRef](#)]
8. Wenjie, C.; Ådnanses, A.K.; Hansen, J.F.; Lindtjørn, J.O.; Tianhao, T. Super-capacitors based hybrid converter in marine electric propulsion system. In Proceedings of the The XIX International Conference on Electrical Machines—ICEM 2010, Rome, Italy, 6–8 September 2010; pp. 1–6.
9. Minami, S.; Hanada, T.; Matsuda, N.; Ishizu, K.; Nishi, J.; Fujiwara, T. Performance of a Newly Developed Plug-in Hybrid Boat. *J. Asian Electr. Veh.* **2013**, *11*, 1653–1657. [[CrossRef](#)]
10. Bellache, K.; Camara, M.B.; Dakyo, B. Hybrid Electric Boat based on variable speed Diesel Generator and lithium-battery—Using frequency approach for energy management. In Proceedings of the 2015 Intl Aegean Conference on Electrical Machines & Power Electronics (ACEMP), 2015 Intl Conference on Optimization of Electrical & Electronic Equipment (OPTIM) & 2015 Intl Symposium on Advanced Electromechanical Motion Systems (ELECTROMOTION), Side, Turkey, 2–4 September 2015; pp. 744–749.
11. Camara, M.B.; Dakyo, B. Real time energy management for hybrid electric boat applications—Using variable speed diesel generator and lithium-battery. In Proceedings of the 2016 IEEE International Conference on Automation, Quality and Testing, Robotics (AQTR), Cluj-Napoca, Romania, 19–21 May 2016; pp. 1–6.
12. Ortuzar, M.; Moreno, J.; Dixon, J. Ultracapacitor-Based Auxiliary Energy System for an Electric Vehicle: Implementation and Evaluation. *IEEE Trans. Ind. Electron.* **2007**, *54*, 2147–2156. [[CrossRef](#)]
13. Jung, H.; Wang, H.; Hu, T. Control design for robust tracking and smooth transition in power systems with battery/supercapacitor hybrid energy storage devices. *J. Power Sources* **2014**, *267*, 566–575. [[CrossRef](#)]
14. Choi, M.E.; Kim, S.W.; Seo, S.W. Energy Management Optimization in a Battery/Supercapacitor Hybrid Energy Storage System. *IEEE Trans. Smart Grid* **2012**, *3*, 463–472. [[CrossRef](#)]
15. Li, Q.; Chen, W.; Li, Y.; Liu, S.; Huang, J. Energy management strategy for fuel cell/battery/ultracapacitor hybrid vehicle based on fuzzy logic. *Int. J. Electr. Power Energy Syst.* **2012**, *43*, 514–525. [[CrossRef](#)]
16. Niu, J.G.; Zhou, S. Fuzzy Logic Control Strategy for an Extended-Range Electric Vehicle. *Appl. Mech. Mater.* **2012**, *220–223*, 968–972. [[CrossRef](#)]
17. Fernández, R.Á.; Caraballo, S.C.; Cilleruelo, F.B.; Lozano, J.A. Fuel optimization strategy for hydrogen fuel cell range extender vehicles applying genetic algorithms. *Renew. Sustain. Energy Rev.* **2018**, *81*, 655–668. [[CrossRef](#)]
18. Liu, D.; Wang, Y.; Zhou, X.; Lv, Z. Extended range electric vehicle control strategy design and multi-objective optimization by genetic algorithm. In Proceedings of the 2013 Chinese Automation Congress, Changsha, China, 7–8 November 2013; pp. 11–16.
19. Zhao, J.; Ma, Y.; Zhang, Z.; Wang, S.; Wang, S. Optimization and matching for range-extendors of electric vehicles with artificial neural network and genetic algorithm. *Energy Convers. Manag.* **2019**, *184*, 709–725. [[CrossRef](#)]
20. Xi, L.; Zhang, X.; Sun, C.; Wang, Z.; Hou, X.; Zhang, J. Intelligent Energy Management Control for Extended Range Electric Vehicles Based on Dynamic Programming and Neural Network. *Energies* **2017**, *10*, 1871. [[CrossRef](#)]
21. Salmasi, F.R. Control Strategies for Hybrid Electric Vehicles: Evolution, Classification, Comparison, and Future Trends. *IEEE Trans. Veh. Technol.* **2007**, *56*, 2393–2404. [[CrossRef](#)]
22. Du, J.; Chen, J.; Song, Z.; Gao, M.; Ouyang, M. Design method of a power management strategy for variable battery capacities range-extended electric vehicles to improve energy efficiency and cost-effectiveness. *Energy* **2017**, *121*, 32–42. [[CrossRef](#)]
23. Villani, M.; Shiledar, A.; Zhao, T.; Lana, C.; Le, D.; Ahmed, Q.; Rizzoni, G. Optimal Energy Management Strategy for Energy Efficiency Improvement and Pollutant Emissions Mitigation in a Range-Extender Electric Vehicle. In Proceedings of the 2021 15th International Conference on Engines & Vehicles, Capri, Naples, Italy, 12–16 September 2021.
24. Sun, L.; Walker, P.; Feng, K.; Zhang, N. Multi-objective component sizing for a battery-supercapacitor power supply considering the use of a power converter. *Energy* **2018**, *142*, 436–446. [[CrossRef](#)]
25. Nitta, N.; Wu, F.; Lee, J.T.; Yushin, G. Li-ion battery materials: Present and future. *Mater. Today* **2015**, *18*, 252–264. [[CrossRef](#)]
26. Cai, Q.; Brett, D.J.L.; Browning, D.; Brandon, N.P. A sizing-design methodology for hybrid fuel cell power systems and its application to an unmanned underwater vehicle. *J. Power Sources* **2010**, *195*, 6559–6569. [[CrossRef](#)]

27. Bauman, J.; Kazerani, M. An Analytical Optimization Method for Improved Fuel Cell–Battery–Ultracapacitor Powertrain. *IEEE Trans. Veh. Technol.* **2009**, *58*, 3186–3197. [[CrossRef](#)]
28. Reiter, C.; Wassiliadis, N.; Wildfeuer, L.; Wurster, T.; Lienkamp, M. Range Extension of Electric Vehicles through Improved Battery Capacity Utilization: Potentials, Risks and Strategies. In Proceedings of the 2018 21st International Conference on Intelligent Transportation Systems (ITSC), Maui, HI, USA, 4–7 November 2018; pp. 321–326.
29. Guan, J.-C.; Chen, B.-C.; Wu, Y.-Y. Design of an Adaptive Power Management Strategy for Range Extended Electric Vehicles. *Energies* **2019**, *12*, 1610. [[CrossRef](#)]
30. Yao, M.; Zhu, B.; Zhang, N. Adaptive real-time optimal control for energy management strategy of extended range electric vehicle. *Energy Convers. Manag.* **2021**, *234*, 113874. [[CrossRef](#)]
31. Phipps, W.; Harrison, M.J.; Duke, R.M. Three-Phase Phase-Locked Loop Control of a New Generation Power Converter. In Proceedings of the 2006 1ST IEEE Conference on Industrial Electronics and Applications, Singapore, 24–26 May 2006; pp. 1–6.
32. Tian, J.; Li, S.; Liu, X.; Yang, D.; Wang, P.; Chang, G. Lithium-ion battery charging optimization based on electrical, thermal and aging mechanism models. *Energy Rep.* **2022**, *8*, 13723–13734. [[CrossRef](#)]
33. Barzacchi, L.; Lagnoni, M.; Rienzo, R.D.; Bertei, A.; Baronti, F. Enabling early detection of lithium-ion battery degradation by linking electrochemical properties to equivalent circuit model parameters. *J. Energy Storage* **2022**, *50*, 104213. [[CrossRef](#)]
34. Pulavarthi, C.; Kalpana, R.; Parthiban, P. State of Charge estimation in Lithium-Ion Battery using model based method in conjunction with Extended and Unscented Kalman Filter. In Proceedings of the 2020 International Conference on Power Electronics and Renewable Energy Applications (PEREA), Kannur, India, 27–28 November 2020; pp. 1–6.
35. Liu, X.; Xu, W.; Zheng, D.; Li, Z.; Zeng, Y.; Lu, X. Carbon cloth as an advanced electrode material for supercapacitors: Progress and challenges. *J. Mater. Chem. A* **2020**, *8*, 17938–17950. [[CrossRef](#)]
36. Cheng, X.F.; Liu, C.; Wang, D.; Zhang, Y. State-of-the-Art Review on Soft-Switching Technologies for Non-Isolated DC–DC Converters. *IEEE Access* **2021**, *9*, 119235–119249. [[CrossRef](#)]
37. Mumtaz, F.; Yahaya, N.Z.; Meraj, S.T.; Singh, B.; Kannan, R.; Ibrahim, O. Review on non-isolated DC-DC converters and their control techniques for renewable energy applications. *Ain Shams Eng. J.* **2021**, *12*, 3747–3763. [[CrossRef](#)]
38. Park, S.J.; Park, J.W.; Kim, K.H.; Kang, F.S. Battery Energy Storage System With Interleaving Structure of Dual-Active-Bridge Converter and Non-Isolated DC-to-DC Converter With Wide Input and Output Voltage. *IEEE Access* **2022**, *10*, 127205–127224. [[CrossRef](#)]
39. Mecke, R. Permanent magnet synchronous motor for passenger ship propulsion. In Proceedings of the 2009 13th European Conference on Power Electronics and Applications, Barcelona, Spain, 8–10 September 2009; pp. 1–10.
40. Thome, R.J.; Bowles, E.; Reed, M. Integration of Electromagnetic Technologies Into Shipboard Applications. *IEEE Trans. Appl. Supercond.* **2006**, *16*, 1074–1079. [[CrossRef](#)]
41. Zhonghui, Z.; Jiao, S. Matlab-based permanent magnet synchronous motor vector control simulation. In Proceedings of the 2010 3rd International Conference on Computer Science and Information Technology, Chengdu, China, 9–11 July 2010; pp. 539–542.
42. Qiangqiang, L.; JianGuo, S.; Jie, D.; PengTao, M. Research of the Method for Position Detection of the Rotor in the Interior Permanent Magnet Synchronous Motor. In Proceedings of the 4th International Conference on Mechatronics, Materials, Chemistry and Computer Engineering, Xi’an, China, 12–13 December 2015.
43. Cárdenas, R.; Clare, J.; Wheeler, P. 4-leg matrix converter interface for a variable-speed diesel generation system. In Proceedings of the IECON 2012—38th Annual Conference on IEEE Industrial Electronics Society, Montreal, QC, Canada, 25–28 October 2012; pp. 6044–6049.
44. Adámek, M.; Toman, R. Range extender ice multi-parametric multi-objective optimization. *MECCA J. Middle Eur. Constr. Des. Cars* **2021**, *18*, 10. [[CrossRef](#)]
45. Al-Adsani, A.S.; Jarushi, A.M.; Beik, O. ICE/HPM generator range extender for a series hybrid EV powertrain. *IET Electr. Syst. Transp.* **2020**, *10*, 96–104. [[CrossRef](#)]
46. Zhancheng, W.; Weimin, L.; Yangsheng, X. A novel power control strategy of series hybrid electric vehicle. In Proceedings of the 2007 IEEE/RSJ International Conference on Intelligent Robots and Systems, San Diego, CA, USA, 29 October–2 November 2007; pp. 96–102.
47. Barsali, S.; Miulli, C.; Possenti, A. A control strategy to minimize fuel consumption of series hybrid electric vehicles. *IEEE Trans. Energy Convers.* **2004**, *19*, 187–195. [[CrossRef](#)]

Disclaimer/Publisher’s Note: The statements, opinions and data contained in all publications are solely those of the individual author(s) and contributor(s) and not of MDPI and/or the editor(s). MDPI and/or the editor(s) disclaim responsibility for any injury to people or property resulting from any ideas, methods, instructions or products referred to in the content.